A review of synthesis method and application of MXenes as host in lithium metal anodes

LI Feng, ZHAO Zhen-xin, CHEN Xu, LI Wen-yi, WANG Xiao-min*

（*College of Materials Science and Engineering*, *Taiyuan University of Techenoogy*, *Taiyuan* 030024, *China*）

Abstract: Severe dendritic growth and volume expansion are easily induced during the cycling process when lithium metal is used as an anode electrode directly. These problems cause the solid electrolyte interface (SEI) layer to break and re-form, which consumes the active lithium metal and electrolyte, thereby reducing the Coulomb efficiency and rapid capacity. Designing a host matrix with rapid mass transfer and enough storage space to promote lithium homogeneous deposition, hence reducing the repeated SEI growth and the formation of dead lithium, is an effective method to address the concerns mentioned above issues. MXenes with two-dimensional layered structures have been regarded as feasible hosts for stabilizing lithium due to their superior electrical conductivity, sizeable interlayer space, abundant lithiophilic surface functional groups, and excellent mechanical properties. In this review, we first summarized the multiple synthesis methods of MXenes, including etching the precursor MAX phase, chemical vapor deposition, UV-induced etching, and mechanochemical et al. Various synthesis methods would induce different surface termination and lamellar structures, affecting lithium metal nucleation and growth behavior. Subsequently, pure MXene, MXene-carbon and MXene-non carbon hybrid compounds applied for lithium metal anode hosts were introduced, focusing on alleviating noticeable volume changes and inhibiting lithium dendrite growth. Finally, some modification strategies and potential research prospects were summarized and prospected.

Key words: MXene; 2D materials; Synthetize; Lithium anodes; Carbon hybridization

1 Introduction

Rapid development of global economy and population increase have intensified energy demands. Additionally, the large consumption of traditional non-renewable fossil fuels makes the problems of energy depletion and environmental pollution increasingly prominent[1–6]. To continue to implement the concept of sustainable development, it is urgent to develop and utilize renewable energy (hydropower, wind energy, biomass energy and etc.)[7–8]. Among these new energy sources, research on electrochemical energy is essential, and the development and utilization of batteries have attracted widespread attention. Lithium-ion batteries (LIBs) are popular due to their high voltage, long cycle life, low self-discharge and high energy density[9–13]. However, the energy density of LIBs has reached a bottleneck of 250-300 Wh kg^{-1} associated with the limited theoretical capacity of the carbon anode material, which is inadequate to keep up with the growing energy requirements[14]. Lithium metal, known as the “Holy Grail” anode material, has stimulated the enthusiasm of researchers, which is attributed to high theoretical specific capacity (~3 860 Ah kg^{-1}), low redox potential (−3.04 V, relative to standard hydrogen electrode) and low density (0.53 g cm^{-3})[15–17]. It has been reported that the energy density of the full cell reach ~440 Wh kg^{-1} when lithium metal is used as anode matched with LMO (lithium transition metal oxide) cathode[18], which is far higher than that of advanced LIBs (250 Wh kg^{-1}). In addition, the lithium-free cathode could be easily matched when the anode is lithium metal, which is beneficial to expand the lithium battery system further. However, the irreversible continuous reaction between high active lithium metal and electrolyte results in the formation of thick solid electrolyte interphase (SEI) layer on the surface of lithium metal, which increases internal resistance, thus reducing Coulombic efficiency and shortening cycle life. Besides, the hostless nature of lithium metal anode (LMA) would produce unlimited volume expansion during cycling and the SEI film is too fragile to inhibit the significant change of anode. Furthermore, lithium ions in the electrolyte gets elec-

Received date: 2023-05-09; **Revised date:** 2023-06-15

Corresponding author: WANG Xiao-min, Ph.D., Professor. E-mail: wangxiaomin@tyut.edu.cn

Author introduction: LI Feng, Ph.D. E-mail: lizhuzhu09@163.com

trons to deposit on the surface of lithium metal during the charging process, which is easy to form moss-like, needle-like or whisker-like dendrites[19–23]. On the one hand, lithium dendrites would provide sites for lithium preferential deposition, leading to excessive consumption of lithium and electrolyte. On the other hand, lithium dendrites are prone to form "dead lithium". Severe dendrite growth would pierce the diaphragm and cause short circuits[24–26]. Multiple strategies have been proposed to address these issues, which are devoted to constructing lithiophilic surfaces and expanding Li-ion transfer channels[27–31]. Represented by graphene, two-dimensional (2D) layered materials present excellent physical properties and chemical stability[32–34], which is conducive to achieving stable and dendrite-free LMAs.

MXene, a novel kind of 2D transition metal carbides or nitrides (general formula: $M_{n+1}X_nT_x$, where M represents early transition metal; X represents C and/or N; n=1, 2, 3; T represents termitransition group, such as —O, —F, —Cl, —OH), has been one of the promising hosts for LMA[35–37]. Firstly, A single-layer structure MXene sheet is easily processed into a well-designed cell structure by various means, containing coating[38–40], layer-on-layer stacking[41–42], and 3D printing[43–44], etc. The adjustable interlayer space of MXene layers provides sufficient space for Li^+ transport to guide uniform Li deposition and growth. MXene was firstly reported to be applied as Li hosts through repeated scrolling and folding processes in 2017. Based on the lithiophobic nature of the atomic layer, the nucleation and growth behavior of lithium dendrites are effectively controlled, which limits the electroplating of lithium within nanoscale gaps, resulting an excellent cycling stability[41]. In addition, Gong et al.[45] deposited g-C_3N_4 layer on the $Ti_3C_2T_x$ surface, which not only provided sufficient lithium affinity sites but also prevented lithium metal from being continuously corroded by electrolytes. Full cells matched with LFP cathode achieved high capacity retention of 85.5% after 320 cycles at 0.5 C. Secondly, excellent electronic conductivity and fast ion diffusion coefficient ensure fast electrochemical kinetics during the lithium plating/stripping process. Third, the abundant lithiophilic functional groups on the surface of MXene provide nucleation sites for Li uniform deposition. Lai et al.[46] reported MXene@COF heterostructures with high crystallinity, graded porosity and high conductivity. The lithiated channel enabled fast Li^+ transport and accurate Li nucleation, which provided a feasible for rapid charging of anodes without dendrites. Furthermore, MXene materials possess synergies in mechanical strength and flexibility, which alleviates the volume expansion of lithium metal anode. Atomic force microscope (AFM) nanoindentation test showed that the Young's modulus and tensile strength of single layer $Ti_3C_2T_x$ MXene reach 330 and 17.3 GPa, respectively. Besides, the advantages of lightweight, low cost and stable chemical properties also assist MXene in adopting on lithium metal anode[36, 47–49].

In this review, the recent advancements towards MXene-based LMA are discussed systematically, focusing on summarizing synthesis methods and application of MXene hosts for LMAs (Fig. 1), as well as prospects towards the commercial applications of MXene-based LMAs.

2 Synthesis methods of MXenes

MXenes are usually obtained from layered MAX (M is early transition metal, such as Ti, Mo, V, etc; A

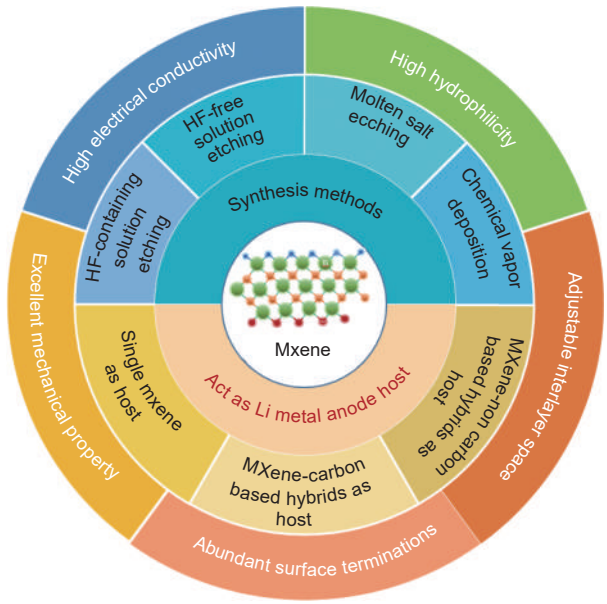

Fig. 1 Overview of representative synthesis methods of MXenes and application as lithium metal anode host

is an element from IIIA or IVA group, such as Al, Si, Ga, etc; X represents N and/or C) phase precursors[50–51]. In MAX, M and X are combined by strong covalent bond and ionic bond, while M connects with A through weak interacted metal bond, so M-A bond is easier to be destroyed with the help of chemical etchants. So far, over 30 MXenes with different termination groups have been produced through experiments, such as O-terminated MXenes (e.g. Ti_2CO_2), F-terminated MXenes (e.g. $ScCF_2$). S-terminated MXenes (e.g. V_2NS_2), and Cl-terminated MXenes (e.g. $Ti_3C_2Cl_2$) et al. And theoretical predictions may reach over 100 types[52]. The reported synthesis methods contain hydrofluoric-based solution etching method, hydrofluoric-free solution etching method, molten salt etching method, and chemical vapor deposition (CVD) method, et al.

2.1　Hydrofluoric-based solution etching method

In 2011, Gogotsi and co-workers[53] successfully prepared the first $Ti_3C_2T_x$-MXene from Ti_3AlC_2 using hydrofluoric (HF) acid solution at room temperature. This method selectively etches the Al-layer atoms based on the strong acidity and oxidation of HF, followed by delamination into single-layer flakes (Fig. 2a). The concentration of HF significantly affects the morphology of MXene. HF solution with high concentrations could produce more defects, leading to the well separated layered structures but lower yields. Besides, etching time is another crucial parameter. Generally, $M_{n+1}C_nT_x$-MXene with a high n value requires an extended etching time. For example, the time for etching $Mo_2Ti_2AlC_3$ (n=3) is twice than that of Mo_2TiAlC_2 (n=2) under the same etching conditions[54]. Because of the low reduction potential for Al element, MXenes are usually obtained from MAX phases containing Al and the central etching reaction equation is as follows[55]:

$$M_{n+1}AlX_n+3HF\rightarrow M_{n+1}X_n+AlF_3+3/2H_2 \quad (1)$$

$$M_{n+1}X_n+2H_2O\rightarrow M_{n+1}X_n(OH)_2+H_2 \quad (2)$$

$$M_{n+1}X_n+2HF\rightarrow M_{n+1}X_nF_2+H_2 \quad (3)$$

At first, MAX precursor reacts with HF to generate MXene phase (Reaction (1)), then Reactions (2) and (3) are generated different surface terminals (−F, −O, −OH, et al.).

The high levels of acidity and toxicity of HF challenge the experimental conditions and experimental operation, leading to difficulties in its widespread use. As a result, researchers have focused on searching for milder etchants that could replace HF in direct etching of MAX phase. To this end, a novel approach involving the *in-situ* synthesis of HF has been proposed, which involves mixing hydrochloric acid (HCl) and lithium fluoride (LiF). This method could

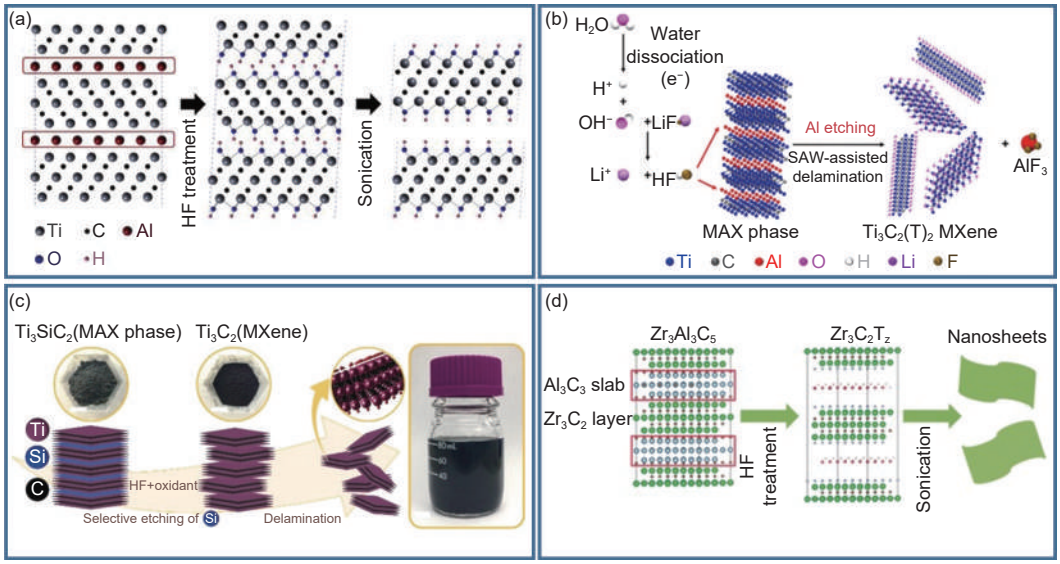

Fig. 2　(a) Schematic of the preparation of MXene by HF acid solution etching[53]. (b) Schematic of the synthesis of $Ti_3C_2(T)_z$ MXene through selective etching with HF generated in-situ protons and LiF[57]. (c) Schematic of etching Si to synthesize MXene[62]. (d) Schematic of using HF to selectively remove Al_3C_3 for preparing Ti-free based $Zr_3C_2T_z$[63]. Reprinted with permission

significantly improve the efficiency and safety of the etching process. Feng et al.[56] mixed 2 mL deionized water and 10 mL HCl and then added 0.8 g LiF and stirred for 30 min, followed by the addition of Ti_3AlC_2 to fabricate MXene. More novelty, Ghaza et al.[57] dissociated the solution to produce protons under the excitation of megahertz-level frequency sound, then the proton combined with the F^- in LiF to form HF (Fig. 2b). *In-situ* synthesis HF methods show the characteristics of low corrosiveness, high stripping rate and few defects. It is reported that MXenes have higher volume fraction of —O terminal groups but fewer F— containing functional groups through *in-situ* synthesis HF etching method. Afterwards, other fluorides (NaF, KF, CaF_2 and NH_4F)/difluorides ($NaHF_2$, KHF_2 and NH_4HF_2) mixed with HCl or sulfuric acid also been confirmed to be used for *in situ* synthesis of HF to etch MAX phase[58–61]. For a long time, MXene could only be produced by MAX phase containing Al. But Ti_3AlC_2 is costly, resulting in limited application in mass production. In 2018, Alhabeb and co-workers[62] reported the synthesis of titanium carbide (MXene) by selectively etching Si from Ti_3SiC_2 precursor phase using HF and H_2O_2 etchant (Fig. 2c). MXene prepared by etching Si has higher oxidation resistance, which expanded the applications area of MXene materials. Except Ti-based MXene, Du's team[63] used HF to selectively remove Al_3C_3 to prepare $Zr_3C_2T_z$ without Ti base (Fig. 2d). Subsequently, Cr_2TiC_2, Ti_2C, Mo_2C and other MXene materials were synthesized successively, which opens new ways for large-scale synthesis of MXene.

The structure of MXene obtained by the HF etching method is of loose accumulation with incompletely peeled layers, thus, further intercalation and sonication treatment are needed. Various inorganic/organic and ions/molecules are used as pillars to weaken MX bonds and increase the layer spacing. Mashtalir et al.[64] mixed hydrazine and N, N-dimethylformamide (DMF) in MXene, followed by sonication treatment, resulting in the expended layer spacing and single-layer MXene in sub-micrometer sizes. Note that the ultrasonic treatment time needs to be controlled reasonably, otherwise MXene sheets display significant defects under long-time ultrasonic treatment.

2.2 Hydrofluoric-free solution etching method

Hydrofluoric etchants with strong acidity and toxicity are not adapted to large-scale application and fluoric-based etchants would introduce inert F-terminal, which affects the performance of MXene[36,47]. Thus, hydrofluoric-free etching methods arouse the research interests. Feng et al.[65] obtained $Ti_3C_2T_x$ (MXene) by etching Ti_3AlC_2 in a mixed solution of NH_4Cl and tetramethylammonium hydroxide (TMA·OH) (Fig. 3a). The strong binding energy between Cl^- and Al results the breakage of Ti-Al bonds. The etching process was greatly promoted by the *in-situ* intercalation of ammonium hydroxide (NH_4OH). Ultimately, carbide flakes with large size of 18.6 μm and high yields of 90% were extracted, more importantly without any F-terminal groups. Alkali is another etching agent owing to the strong binding ability with Al. Zhang and co-worker[66] applied 27.5 m NaOH assisted hydrothermal of 270 °C etching under an argon atmosphere and successfully prepare $Ti_3C_2T_x$ with the purity of 92% (Fig. 3b). In this process, some oxides/hydroxides could be produced on the surface of MXene, which considerably affects the reaction kinetics. So, acid treatment is needed after etching.

2.3 Molten salt etching method

Some water-soluble residual products would be generated when using aqueous etchants, which affects the purity of MXene. In addition, the precursors used to prepare MXene are mainly Al-based MAX phases, accounting for only about 20% of the MAX phase materials. Therefore, it is also essential to develop a technology that could etch the remaining 80% members of the MAX phase family into MXene materials. Li et al.[67] synthesized Ti_3ZnC_2 in $ZnCl_2$ molten salt at 500 °C, based on the strong Lewis acidity of $ZnCl_2$ molten salt, *via* a replacement reaction mechanism. However, as the ratio of MAX and $ZnCl_2$ increases, Ti_3ZnC_2 could be converted into $Ti_3C_2Cl_2$-MXene (Fig. 4a), which leads to uncontrollable experiment.

By adjusting the combination of MAX precursor and Lewis acid, Huang's team[68] designed an etching method that element A is directly oxidation-reduction coupled with the positive ions in Lewis acid molten salts, which enables to predict the reactivity of MAX in molten salt and thus increase the yields of MXene (Fig. 4b). Lewis acid cations with high redox potentials could effectively oxidize the A-layer atoms with low redox potentials in the etched MAX phase. Thus, suitable Lewis acids could be selected to synthesize

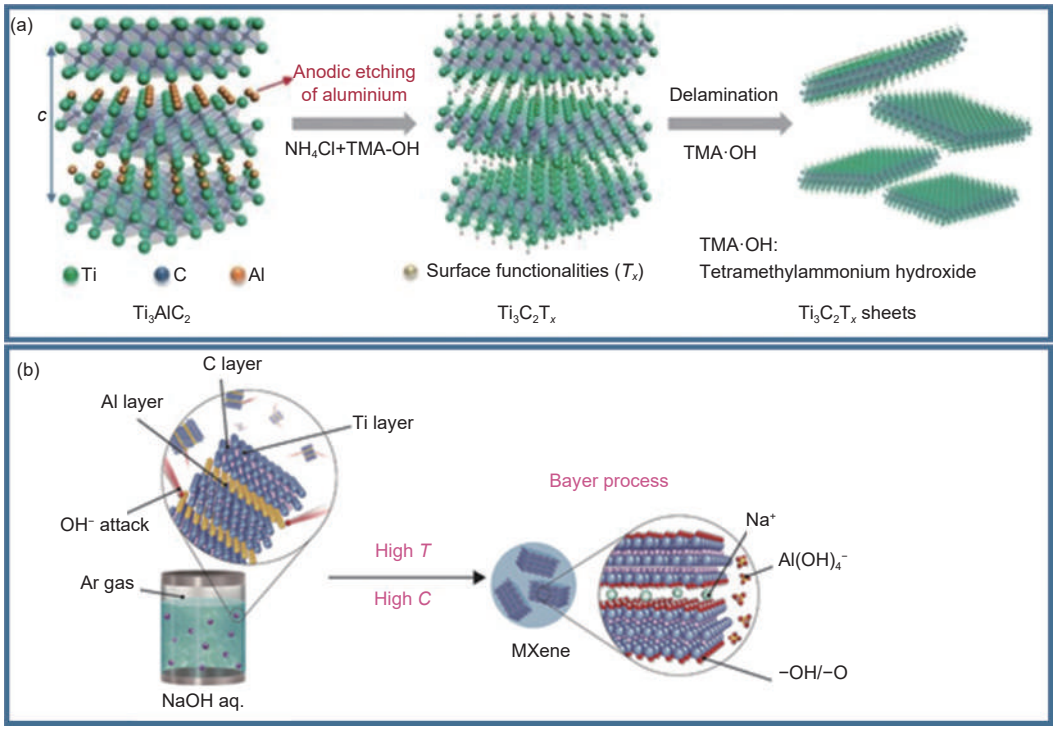

Fig. 3　(a) Schematic of preparing $Ti_3C_2T_x$-MXene in mixed solution of NH_4Cl and TMA·OH[65]. (b) Schematic of NaOH-assisted hydrothermal etching to prepare $Ti_3C_2T_x$[66]. (Reprinted with permission)

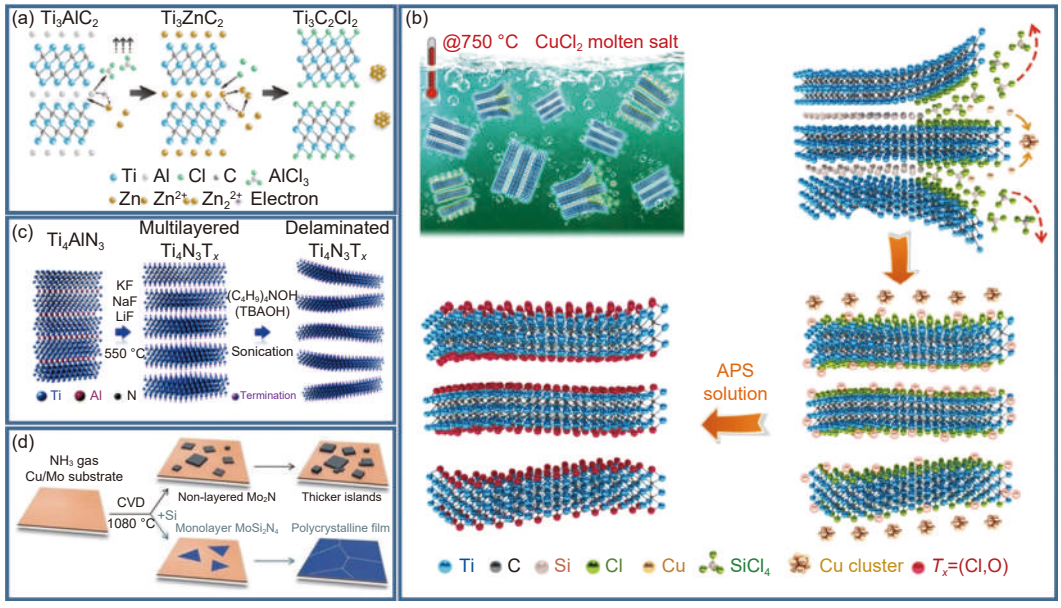

Fig. 4　(a) Schematic of synthesizing Ti_3AlC_2 in $ZnCl_2$ molten salt[67]. (b) Schematic of MXene preparation by oxidation-reduction method of cation coupling of element A and Lewis acid molten salt[68]. (c) Schematic of preparing Ti_4N_3-based MXene[69] (d) Schematic of introducing Si source to prepare single layer $MoSi_2N_4$ in CVD process[74]. (Reprinted with permission)

various MXenes from unconventional MAX phase precursors containing Si, Zn and Ga, et al.

Compared with acidic aqueous solution treatment, molten salt etching method could not only produce carbides and carbon nitride MXene, but also etch the MAX phase of the nitride base. Gogotsi and colleagues[69] reported a method for preparing Ti_4N_3-based MXene by heating molten salt mixture (LiF∶KF∶NaF=29%∶58%∶12% (mass fraction)), and Ti_4AlN_3 in Ar atmosphere (Fig. 4c). The prepared MXene retains the Ti-N bonds in the layered hexagonal Ti_4N_3 structure. Furthermore, Kamysbayev's team[70] expanded molten salt etchant and synthesized the first MXene by Br-terminated. Br-terminated MXene could be substituted with more functional groups (—O, —S, —Se, —Te) or vacancy sites to effectively control the surface chemistry and properties of MXene materials. On this basis, MXene without terminal groups is promising to be prepared in the near future. In general, molten salt etching has obvious advantages but faces some challenges: (i) The process needs high temperature heating; (ii) Further treatment is needed for purification; (iii) MXene products have numerous defects.

2.4 CVD method

CVD is a bottom-top method and is mainly used to prepare single or few layers of two-dimensional MXene materials. Ren and co-workers[71] fabricated large-area high-quality 2D ultrathin α-Mo_2C crystal with thickness of a few nanometers by CVD method with methane as the carbon source and Cu foil on Mo foil as the substrate under a temperature of 1 085 °C. In addition, the rapid cooling operation after CVD growth is necessary for obtaining clean ultra-thin films without Mo nanoparticles on the surface α-Mo_2C crystal. Besides, CVD method is also confirmed to allow the manufacture of other high-quality 2D transition metal carbide crystals, such as ultra-thin WC and TaC crystals[72], which further expands the system of 2D materials. Wang[73] proposed utilizing the CVD process to grow Mo_2N nitride on a Cu/Mo substrate. However, Hong et al.[74] discovered that the Mo_2N generated through this approach exhibited non-layered stacking. To address this issue, introducing a Si source into the CVD process produces a centimeter-scale, two-dimensional, single-layer $MoSi_2N_4$ (Fig. 4d).

The single-layer membrane structure of $MoSi_2N_4$ consists of two Si-N bilayers sandwiched with MoN_2 layers, which exhibits high mechanical strength and environmental stability. The CVD method is favorable due to its low cost, ability to cover large surface areas, and precise control over surface termination, morphology, and particle size distribution. However, it typically necessitates high temperature conditions, which may create difficulty during experimental operation. In quite recent years, some novel synthesis routes have been proposed by researchers, such as UV-induced selective etching method[75], mechanochemical (MC) method[76] and a one-pot molten salt electrochemical etching method[77], et al. The structural characteristics and defects of MXene depend heavily on the synthesis methods. Therefore, selecting etchants and routes is crucial for improving the performance of MXene and developing new MXene components.

3 MXenes as host for lithium metal anodes

3.1 Single MXenes as lithium metal anodes host

In 2017, Yang and colleagues[41] introduced 2D MXene as a potential material for lithium metal anodes. Specifically, they utilized a rolling-to-folding mechanical approach to create a flexible, lamellar-structured Ti_3C_2-MXene-Li composite anode (Fig. 5a). Images obtained through SEM analysis revealed that lithium metal was evenly distributed between the ultrathin layers, effectively restricted without the growth of lithium dendrites due to the limited Ti_3C_2 spacing. Additionally, the parallel arrangement of lithium-sparse Ti_3C_2 nanosheets guid the growth directions of lithium metal. In order to evaluate the electrochemical properties of Ti_3C_2 MXene, the cycling performance of the symmetric cell was measured at a current density of 1.0 mA cm^{-1} (Fig. 5b). In the case of Ti_3C_2Li electrode, the voltage distribution is smoother and the

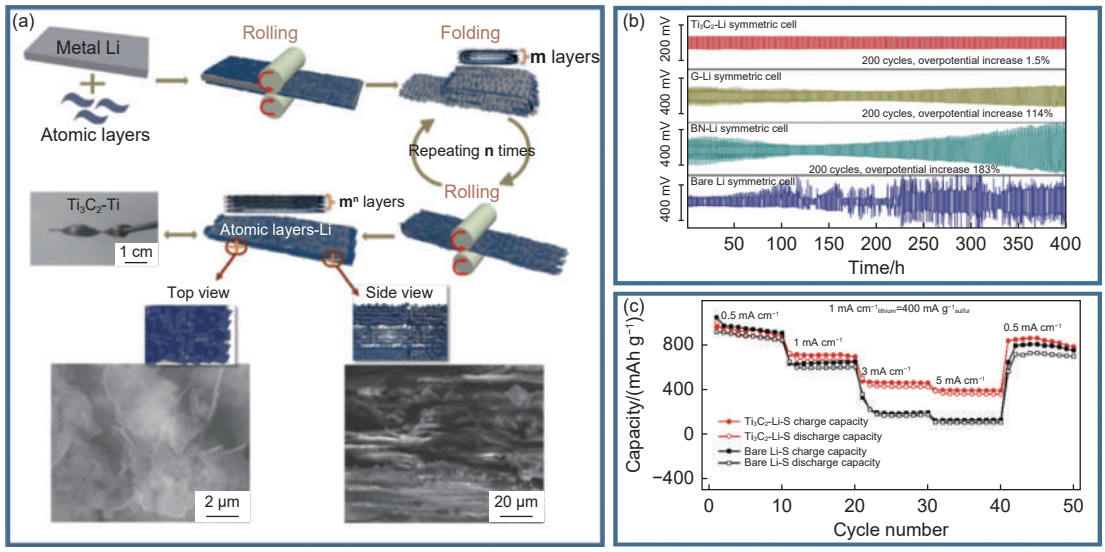

Fig. 5　(a) Preparation flow chart of Ti_3C_2 MXene Li composite anode[41]. (b) Cyclic performance of symmetrical batteries at constant current density of 1.0 mA cm^{-2}[41]. (c) The rate capabilities of Li-S full cells at various current densities from 0.5 to 5 mA cm^{-2}[41]. (Reprinted with permission)

overpotential is only increased by 1.5% after 200 cycles, which is owing to high electrical conductivity, numerous nuclear sites on the surface and large gaps in the lamellar structure. The lithium affinity of Ti_3C_2 MXene could not only effectively prevent the nucleation and growth of lithium dendrites but also promote the deposition of lithium in nano-slice gap, resulting in the low overpotential of 32 mV at 1.0 mA cm^{-2} over 200 cycles. Ti_3C_2-Li electrode yet maintained perfect layered structure during long-time cycling, reflecting robust mechanical strength, which provides an effective barrier for lithium dendrite growth. The full cell (Ti_3C_2-Li as anode and sulfur carbon as cathode) exhibited high reversible capacity (948 mAh g^{-1}) and excellent cycle performance. Even at a high current density of 5.0 mA cm^{-2}, the capacity remained at 360 mAh g^{-1} (Fig. 5c).

In recent years, there has been enthusiastic attention on constructing 3D hosts due to their potential to promote rapid charge transfer of lithium ions, lengthen cycle life and inhibit volume change. However, the conventional horizontal stacking of MXene nanosheets could limit the ion transport rate in the electrode. Chen et al.[78] developed a vertically aligned $Ti_3C_2T_x$-MXene nanosheet array (v-$Ti_3C_2T_x$) as Li metal anode host adopting a facile ice template assisted blade coating method (Fig. 6a). This method is also applicable to the large-scale preparation of electrodes, accelerating the development of lithium metal batteries. The numerous channels between the vertically aligned MXene walls provide significant advantages for electrolyte adsorption and ion transport (Fig. 6b, c), thereby enhancing the rate performance of the electrode. In addition, the abundant O— and F—containing groups on MXenes surface participated in forming a homogeneous SEI layer, which enables dendrite-free lithium deposition and maintains structural stability during the plating/striping process. Furthermore, they demonstrated the nucleation and deposition behaviors of Li metal guided by v-$Ti_3C_2T_x$ electrode using ex-situ SEM characterization. When the Li plating capacity is 1 mAh cm^{-2}, the Li metal is deposited in vertical MXene array channels (Fig. 6d). When the plating capacities were increased to 3 mAh cm^{-2} and 6 mAh cm^{-2}, Li metal filled the vertical channel tightly (Fig. 6e-f). Therefore, the v-$Ti_3C_2T_x$ electrode has excellent Li metal deposition performance at both small and large capacities. To further reveal the advantages of vertical structures, the lithium deposition process was simulated (Fig. 6g). With the prolongation of deposition time, the thickness of the lithium layer increases, but the channel remains stable. As a result, the $Ti_3C_2T_x$-MXene electrode achieved a high Coulombic efficiency of 98.8% after 450 cycles at a fixed areal capacity of 1.0 mAh cm^{-2} at a current density 1 mA cm^{-2}. Impressively, the

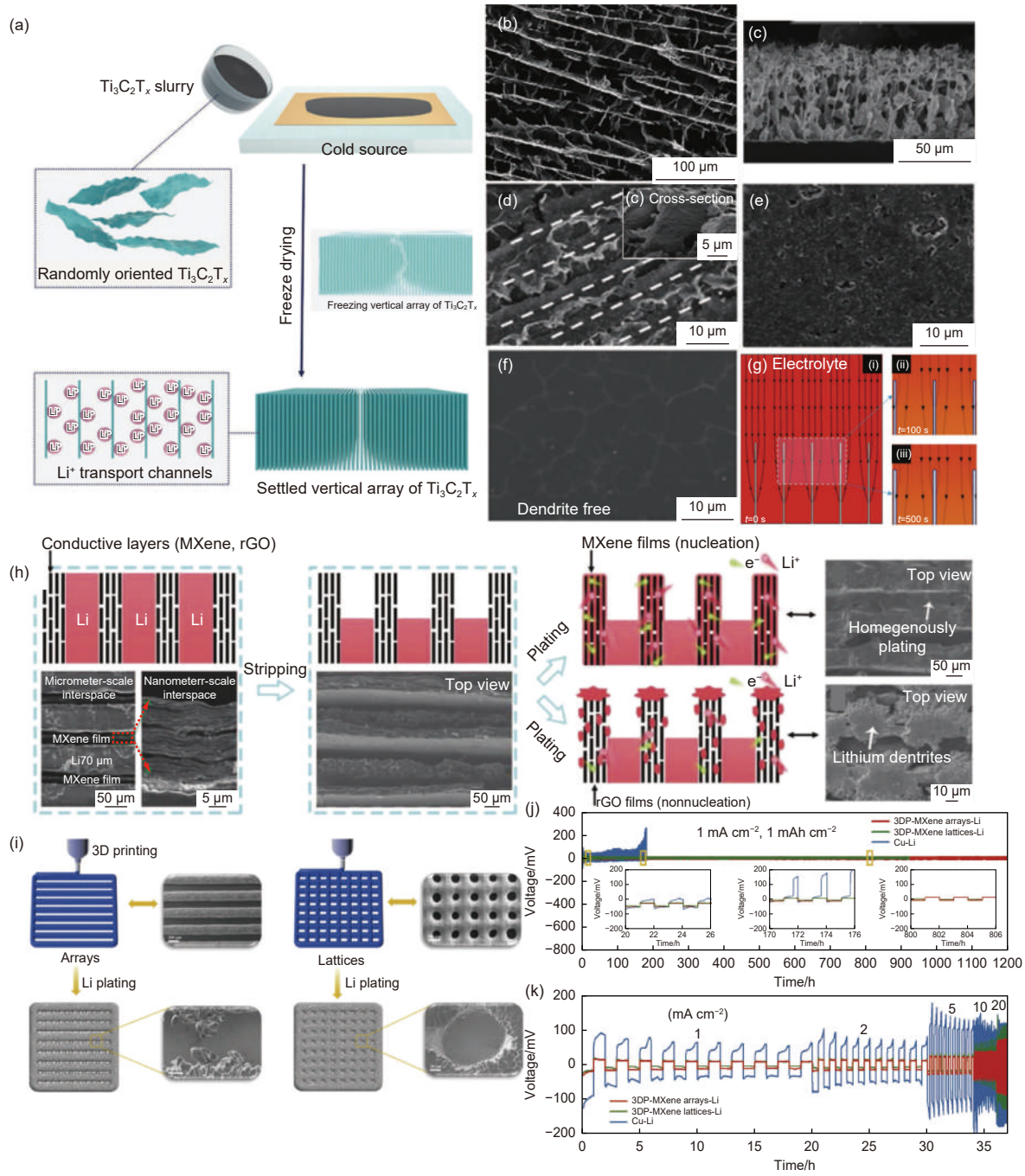

Fig. 6 (a) Schematic of preparing v-$Ti_3C_2T_x$ nanosheet arrays using ice template assisted blade coating method. (b) Top view and (c) cross-section SEM image of v-$Ti_3C_2T_x$ electrodes; SEM characterization of v-$Ti_3C_2T_x$ electrodes after plating different capacities lithium at 1.0 mA cm^{-2}: (d) 1.0 mAh cm^{-2}. (e) 3.0 mAh cm^{-2} (f) 6.0 mAh cm^{-2}. (g) COMSOL simulation of Li deposition on v-$Ti_3C_2T_x$ electrodes[78]. (h) Schematic diagram of peeling and plating states of vertical MXene Li and rGO Li arrays[79]. (j) Schematic diagram of 3D printing MXene array and lattice[80]. (k) Cycling performances of symmetric cells at 1 mA cm^{-2}, 1 mAh cm^{-2}[80]. (m) Rate capabilities from 1 to 20 mA cm^{-2}[80]. (Reprinted with permission)

stable Li plating/peeling behavior could be maintained with a high average CE of 98.5% over 150 cycles even when the area capacity was increased to 5 mAh cm^{-2}, demonstrating the outstanding electrochemical stability, which provided an effective strategy for the construction of lithium metal electrodes for high-current-density and large-capacity operation.

Similarly, Yang's team[79] designed a vertical MXene-Li array with dual-periodic gap, including nanoscale gap in MXene wall and microscale gap between MXene walls. The nanoscale gap in the

MXene wall is conducive to the rapid transmission of lithium ions during stripping and plating. The micron gap between MXene walls could effectively uniform the electric field, suppress the notorious lightning rod effect and volume change. Generally, the more uniform the current distribution on the electrode, the more uniform the metal deposition. Thus, uniform lithium deposition for 1 mAh cm^{-2} was observed in the SEM image (Fig. 6h). As a result, a high-rate capability up to 20 mA cm^{-2}, a low potential of 25 mV, a high capacity of 2 056 mAh g^{-1}, and good cycle stability up to 1 700 h were achieved. 3D host strategies greatly promote the commercial applications of Li metal anodes. But it is a challenge to manufacture mechanically stable 3D MXene frames because of the weak interaction between MXene sheets. 3D printing, an advanced smart manufacturing technology, allows precise control of the shape and structure of electrodes from nanoscale to macroscale, resulting in increased specific energy densities. Meanwhile, the flexible MXene materials are easily sheared under external forces, which is a condition for making 3D printing ink. In view of this, Yang's group[80] fabricated 3D MXene arrays and lattices by extrusion-type 3D printing technology with a high content MXene ink of ~ 300 g L^{-1} (Fig. 6j) and characterized electrochemical properties (Fig. 6k, m). As a result, 3DP-MXene arrays and lattices exhibited a low nucleation overpotential of ~ 15 mV, indicating a significantly reduced lithium plating barrier. Meanwhile, large available interspaces in MXene arrays induce lithium growth parallel to the filaments. Finally, long cycle stability of 1 200 h and high-rate capabilities up to 20 mA cm^{-2} are achieved.

3.2 MXene-carbon based hybrids as lithium metal anodes host

MXene nanosheets produced by traditional methods exhibit limited spatial gaps due to the close stacking arrangement of materials. However, the unique 2D structure and diverse surface functional groups of MXene provide permission for hybridization with other external reagents. Carbon materials with high conductivity, exceptional structural stability and large specific surface area have been confirmed to be effective in widening the Li plating/infusion channels of MXene, while maximize the lithiophilicity and mechanical strength of anodes. The remarkable results achieved by MXene-carbon materials lithium metal hosts have been reported.

Graphene is a desirable lightweight host for LMA due to its outstanding chemical and mechanical stability, large specific surface area and good carrier mobility. However, since the lack of lithiophilicity, primary graphene is not suitable for direct use as a lithium metal host. Therefore, the composites composed of lithiophilic MXene and graphene are expected to act as ideal host of lithium metal anodes. Wu et al.[81] fabricated a MXene/graphene (MG) framework *via* thermal infusion strategy and the fabrication process was shown in Fig. 7a. First, the uniformly mixed suspension of MXene and graphene oxide was obtained through ultrasonic treatment, in which small-sized $Ti_3C_2T_x$ MXene nano-sheets uniformly dispersed on the surface of micron-size graphene oxide sheets. Followed by freeze-dried to form 3D MGO aerogels and then mechanically pressed to obtain laminated MGO film. Once the MGO film contacted with molten lithium, the reduction reaction were induced rapidly to form an interconnected 3D MG nano-porous framework. This 3D frame could significantly inhibit MXene restacking and oxidation, while the robust mechanical property of 3D frame hinders volume expansion of Li deposition. Compared with pure MXenes, —OH terminal groups on the 3D surface disappeared and the —O containing functional groups were retained. The first principles calculation demonstrated that Ti-Li, O-Li and F-Li mixed covalent/ionic bonds play key roles in ensuring uniform lithium metal deposition[82]. The enhanced lithiophilicity and high specific surface area of 259 cm^2 g^{-1} supported MG electrode in achieving an ultrahigh Li content of 92%, a high CE of 99%, a long-term cycling stability over 2 600 h at a high capacity of 5 mAh cm^{-2}. Half of the rGO surface was coated with a pure MXene layer and deposited 1 mAh cm^{-2} Li at a current density of 0.25 mA cm^{-2}. The results showed that lithium-free

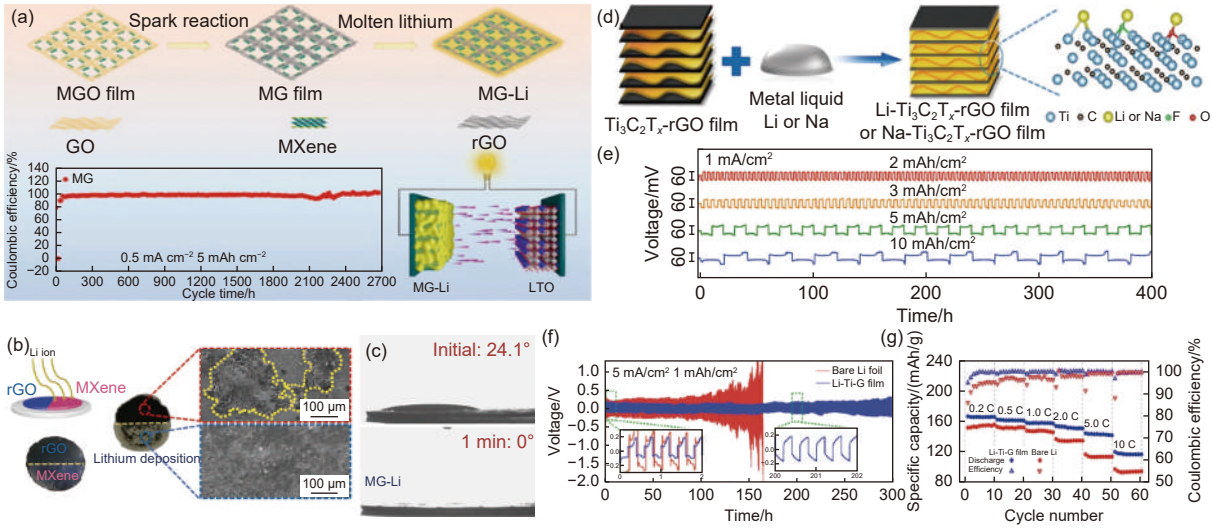

Fig. 7 (a) Schematic of M/G aerogel prepared by thermal infusion strategy process and Coulombic efficiency of MG electrode at a current density of 0.5 mA cm^{-2} with 5 mAh cm^{-2}[81]. (b) Photos and top SEM images of Li deposition on rGO coated MXene and uncoated MXene[81]. (c) The contact angle of electrolyte droplets on MG-Li at the initial time and after 1 min[81]. (d) Schematic illustration of Li-$Ti_3C_2T_x$-rGO preparation[82]. (e) Cycling performances for Li- $Ti_3C_2T_x$-rGO films of stripping/plating capacity of 2, 3, 5 and 10 mAh cm^{-2} at 1 mA cm^{-2} [82]. (f) Cycling of symmetric Li-$Ti_3C_2T_x$-rGO electrodes and bare Li foils for more than 300 h at a current density of 5 mA·cm^{-2}. (g) Rate capability of LFP||Li- $Ti_3C_2T_x$-rGO and LFP||bare-Li cells from 0.2 to 10 C[82]. (Reprinted with permission)

dendrite grow on the surface of the MXene modified part, while irregular Li dendrites were observed in the exposed part without MXene modification (Fig. 7b). Furthermore, the contact angle of electrolyte droplets on MG-Li fell to 0 after 1 min (Fig. 7c), ensuring that Li metal deposits uniformly on the MG scaffold. Consequently, the MG electrode maintains high CEs of ~99% over 2 700 h at 5 mAh cm^{-2}. According to this theory, Cao et al.[82] designed a 3D porous MXene $Ti_3C_2T_x$-reduced graphene oxide (MXene-rGO) matrix with a "building function" as the stable host (Fig. 7d). MXene served as the skeleton and provided wettable surfaces to promote the uniform absorption and nucleation of Li. The graphene oxides acted as isolated nanoanodes, which enabled dendrites generated during repeated stripping/plating processes to be separated and sealed in separate interlayer units, avoiding magnified Li dendrites growth. Based on the first-principles, the —F and —O functional groups on the $Ti_3C_2T_x$ surface exhibited high adsorption energies with lithium of −0.615 and −0.931 eV, respectively. But molten Li did not quickly fill in the entire film when it is injected, which was limited by the tight layered structure of MXene. After standing for 2 min, the GO film ruptured due to intense spark reaction. Finally, the MXene combining with crushed rGO could improve mechanical stability and flexibility, while rGO assisted in expanding the interlayer spacing of MXene and generating porosity to accelerate wetting rate and accommodate a large amount of lithium metal. At a current density of 1 mA cm^{-2}, the Li-$Ti_3C_2T_x$-rGO electrode displayed long cycle lifetimes of 300 and 400 h with deep peel/plating capacities of 5.0 mA cm^{-2} and 10 mAh cm^{-2}, respectively (Fig. 7e). The initial overpotential of Li-$Ti_3C_2T_x$-rGO electrode was ~107 mV and gradually increased to 132 mV after 200 h at 5.0 mA cm^{-2} with 1 mAh cm^{-2} (Fig. 7f). Compared to LFP||bare-Li cells, LFP||Li-$Ti_3C_2T_x$-rGO cells presented a higher discharge specific capacity. Besides, the LFP|| Li-$Ti_3C_2T_x$-rGO cells exhibited fast stability and higher average Coulombic efficiency after 60 cycles (Fig. 7g).

Carbon nanotubes (CNTs) with an inner cavity structure have characteristics of lightweight, flexibility and large specific surface area. Introducing CNTs into MXene not only stabilizes the layer structure but also improves layer-layer spacing. Sun et al.[83] successfully synthesized CNTs@Ti_3C_2 hybrid structure using microwave radiation method. In this structure, the CNTs served as spacers to prevent the restack of

MXene and bridge the gap between Ti_3C_2 intermediate layers. Ti_3C_2 acts as the substrate to provide active sites and promotes the growth of CNTs. The prepared CNTs@Ti_3C_2 maintained a high reversible capacity of 175 mAh g^{-1} at a high rate of 31.25 C. Based on this theory, Xu et al.[84] introduced CNTs into $Ti_3C_2T_x$ to build a crosslinked conductive network, followed by ball-milling method to combine $Ti_3C_2T_x$/CNTs with red phosphorus (P) forming a $Ti_3C_2T_x$/CNTs@P nanohybrid (Fig. 8a). Under the ball-milling shear forces, Ti-O-P chemical bond was formed between P and oxygen containing functional groups on $Ti_3C_2T_x$ nanosheets (Fig. 8b). The P—O bond energy is higher than the P-P bond energy, therefore the formation of Ti-O-P bonds is beneficial to maintain a tight connection between the red P and the substrate, improving structure and cycling stability. Meanwhile, $Ti_3C_2T_x$/CNTs could buffer the large volume change of red P particles during charge/discharge. $Ti_3C_2T_x$/CNTs@P nanometer hybrid material obtained high lithium storage capability of 2 598 mA h g^{-1} at 0.05 C, high Coulombic efficiency of 77% and outstanding long-term cycling stability of 2 078 mA h g^{-1} over 500 cycles. More recently, Yan and co-workers[85] uniformly decorated SnO_2 nanoparticles with highly-lithiophilic and low-nucleation-barrier (~13 mV) on MXene-CNT for uniform Li deposition (Fig. 8c). Lithium ions were preferentially deposited at the bottom of the skeleton and reacted with SnO_2 to produce a Li-Sn alloy phase, providing multiple nucleation sites for Li deposition. Subsequently, the lithium crystals inside the interlayer of MXene would continue to guide the deposition of Li. In addition, the conductivity of the CNT at the top was significantly lower than that of the bottom CNT/MXene/SnO_2 composite film, which further inhibited the growth of Li deposits on the top, resulting in dendrite-free Li anodes. Symmetric cell assembled with Li@CNT/MXene/SnO_2 electrodes achieved stable Li deposition for 1 300 cycles at 10 mA cm^{-2} with an area capacity load of 1 mAh cm^{-2}. With the current density increased to 30 mA cm^{-2}, the voltage hysteresis of the bare Li electrode sharply increased to 350 mV after 260 cycles, which was mainly related to the increased interface resistance caused by the repeatable rupture/reformation of Li dendrites and SEI layers. In contrast, symmetrical batteries with Li@CNT/MXene/SnO_2 electrodes exhibited stable Li plating/stripping behaviors. In situ digital holography technology was used to monitor the change of Li^+ concentration at the electrode/electrolyte interface (Fig. 8d). Note that the blue color at the interface of lithiophilic SnO_2 composite material/electrolyte deepened, corresponding to a decrease in Li^+ concentration with the prolongation of electrodeposition time, which indicated that Li^+ preferentially reduce at the interface of SnO_2/electrolyte to

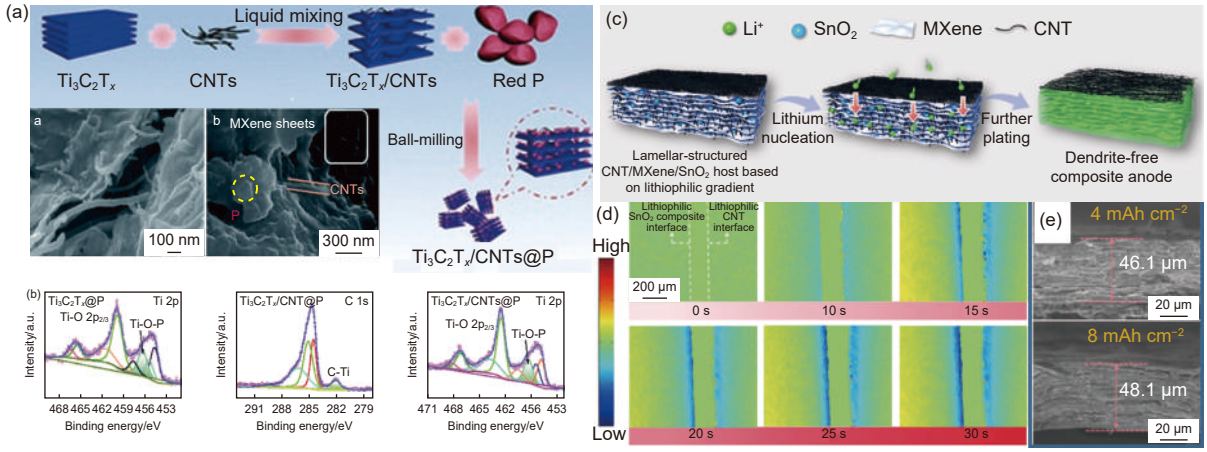

Fig. 8　(a) Schematic of $Ti_3C_2T_x$/CNTs@P nanohybrid as well as SEM imagines of $Ti_3C_2T_x$/CNTs and $Ti_3C_2T_x$/CNTs@P at the bottom left[84]. (b) High resolution XPS spectra of Ti and C[84]. (c) Schematic of Li deposition in the CNT/MXene/SnO_2 composite host[85]. (d) In-situ digital holographic test images of Li metal deposition process in the CNT/MXene/SnO_2 at 10 mA cm^{-2}[85]. (e) SEM morphologies of the CNT/MXene/SnO_2 host with Li plating capacities of 4 mAh cm^{-2} and 8 mAh cm^{-2}[85]. (Reprinted with permission)

form metallic Li. As a result, a high reversible capacity loading of 8 mAh cm^{-2} with only 4.6% volume expansion at 10 mA cm^{-2} was obtained (Fig. 8e). The full battery also exhibited fast-charging capability, excellent cycle stability and high Coulombic efficiency. This work enormously broadened the practical applications of MXene in the durable high-power lithium metal battery field.

Carbon nanofibers are common Li host materials due to good electrical conductivity and high specific surface area, which could effectively reduce the local current density and inhibit the growth of dendrites. Song et al.[86] designed three-dimensional porous $Ti_3C_2T_x$/carbon nanofibers (TCCNFs) foam by annealing MXene/bacterial cellulose (BC)/urea mixture (Fig. 9a). Cationic protonation urea could be strongly absorbed by negatively charged MXene in mild acidic environments, and the abundant functional groups on the surface of MXene could form hydrogen bonds with the hydrophilic groups of bacterial cellulose (BC), resulting in the formation of TCCNFs foam with a stable structure. As shown in Fig.9b and 9c, pores could be observed not only on the cross-section, but also on the MXene sheets. The potential-capacity curve of Li deposited on TCCNFs foam electrode showed that the nucleation overpotential was only 32 mV at 1 mA cm^{-2} (Fig. 9d). Continuing the Li deposition until a short circuit occurred, TCCNFs foam electrode obtained a capacity of 45.7 mAh, which is much higher than that of TCCNFs. In addition, it was observed that Li were evenly distributed along the MXene sheets as well as inside the 3D TCCNFs foam frameworks. The Li^+ migration channels were simulated through finite element analysis (FEA) (Fig. 9e). The results showed that the electric displacement fields on the edges of MXene nanosheets and holes

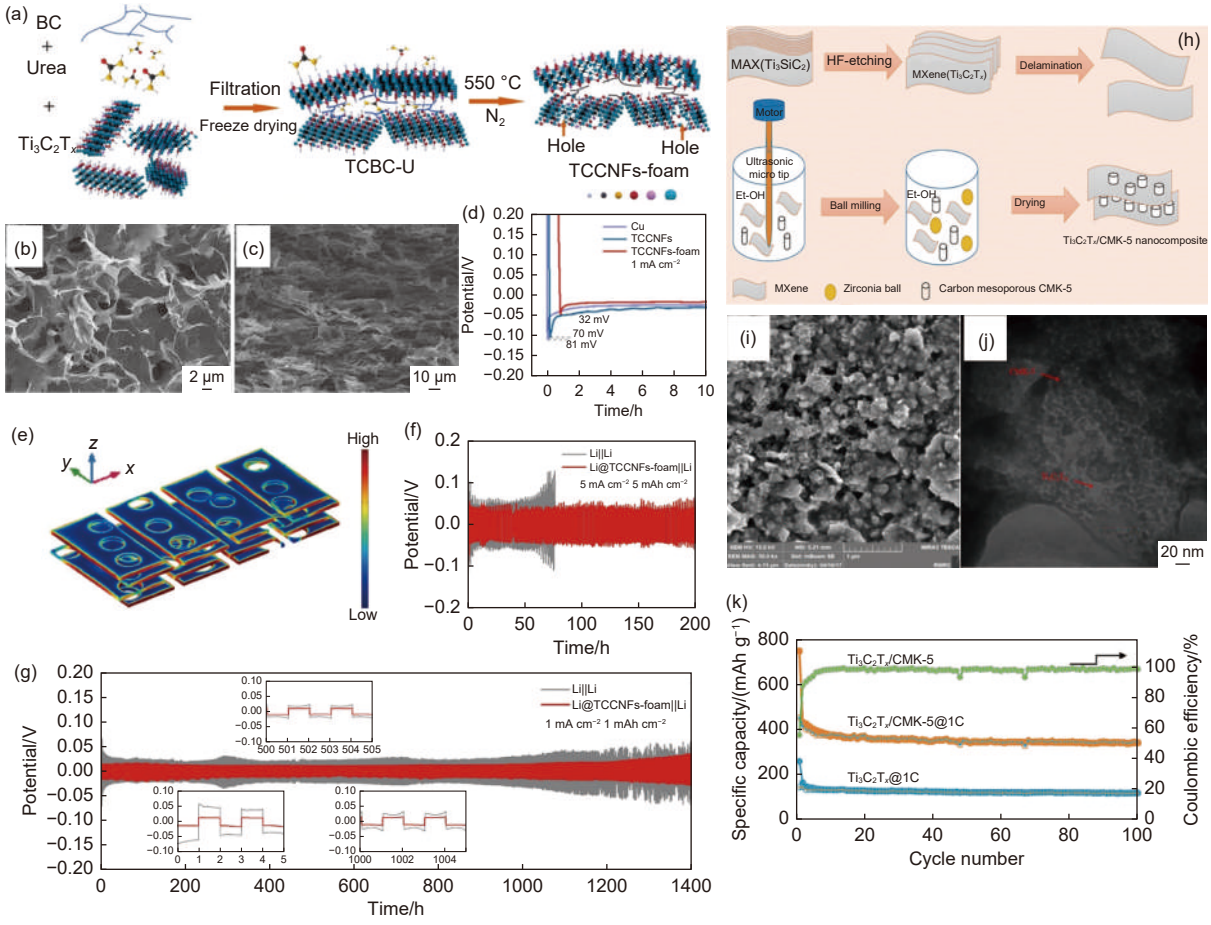

Fig. 9 TCCNFs foam[86]: (a) Preparation schematic, (b) Top-surface and (c) Cross-sectional SEM images. (d) Li deposition curves at 1 mA cm^{-2}. (e) Multiphysics finite elemental analysis of the electric displacement field. (f) Voltage-Time profiles of symmetric cells at 1 mA cm^{-2}, 1 mAh cm^{-2} and (g) 5 mA cm^{-2}, 5 mAh cm^{-2}; $Ti_3C_2T_x$/CMK-5 composite[87]: (h) Preparation schematic. (i) SEM and (j) TEM images. (k) Cycling stability at 1 C. (Reprinted with permission)

were significantly stronger, corresponding to an increase in negative charge concentration at the edges, which could attract lithium ions to form ion channels. The symmetrical cell of Li@TCCNFs foam could effectively run stability for 1 400 and 200 h at 1 mA cm^{-2}, 1 and 5 mAh cm^{-2}, respectively (Fig. 9f and 9g). Further, the as-assembled full cell (Li@TCCNFs-foam as the anode, $LiFePO_4$ as the cathode) delivered 510 cycles and 100 cycles at 2 C and 4 C, respectively.

The capacity and cycle stability of Li anodes could be markedly increased by adding carbon materials to MXenes. On the one hand, carbon materials provide conductive paths for Li ions. On the other hand, it improves structural stability by connecting and supporting MXenes layers. The advantages of regular pore size distribution, adjustable porosity, and excellent chemical and physical stability make ordered mesoporous carbon (OMCs) be practicable selection. Yaftian et al.[87] prepared $Ti_3C_2T_x$/CMK-5 nanocomposite by introducing CMK-5 in to $Ti_3C_2T_x$ layers with fast and simple high-energy, wet ball milling process (Fig. 9h). As seen in Fig. 9j, the special structure of CMK-5 could effectively prevent the stacking of individual $Ti_3C_2T_x$ sheets. TEM image indicated that CMK-5 particles are interconnected between and around thin MXene layers (Fig. 9k). The electrochemical test results displayed a high reversible capacity of 342 mAh g^{-1} at 1 C after 100 cycles (Fig. 9m), which is related to the amplified surface area and stable structure of $Ti_3C_2T_x$/CMK-5 nanocomposite.

3.3 MXene-non carbon based hybrids as lithium metal anodes host

Lithiophilic host design could effectively control lithium deposition to ensure good cycling performance. A strategy for creating lithiophilic surfaces was to use metal nanoseeds with minimal nucleation overpotential. Zn (Zn) is a high-efficiency nucleating agent. Zn doping plays a key role in reducing interfacial resistance and accelerating charge transfer, which in turn promotes redox kinetics and enhances cell reversibility. Recently, Gu et al.[88] immobilized single Zn atoms on MXene layers to control conveniently Li plating behavior (Fig. 10a). The TEM in Fig. 10b showed that single Zn atoms are formed on the top of Zn-MXene nanosheets. Due to a large amount of active Zn sites on the planes and the strong lightning rod effects at the edges, the lithium tended to nucleate uniformly on the Zn-MXene layers and then grew vertic-

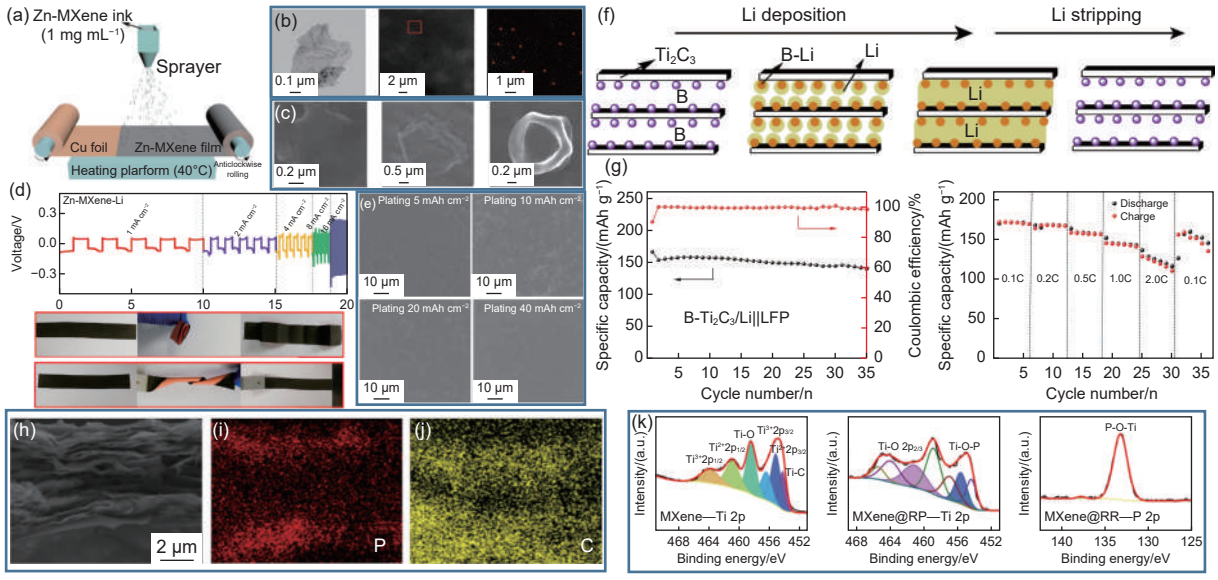

Fig. 10　Zn-MXene nanosheets[88]: (a) Manufacturing schematic. (b) TEM and HAADF-STEM images. (c) SEM images after Li plating with various capacities. (d) Rate capabilities of the Zn-MXene-Li anodes at various current densities (1-16 mA cm^{-2}) and folding and twisting tests. (e) Typical SEM images of Zn-MXene-Li anode at different Li plating levels. (f) Schematic of lithium deposition and stripping process on B-doped $Ti_3C_2T_x$Li electrode[90]. (g) Cycling performance at 0.5 C and rate of full cells assembled with LFP cathode and B-doped $Ti_3C_2T_x$@Li anode[90]. (h) SEM and (i, j) corresponding EDS mapping images of MXene@RP paper. (m) High-resolution XPS spectra of MXene-Ti 2p, MXene@RP-Ti 2p and MXene@RP-P 2p[92]. (Reprinted with permission)

ally to afford bowl-like lithium without lithium dendrites (Fig. 10c). A stable and long-life of 1 200 h as well as good rate capability were achieved for the Zn-MXene-Li anode. The overpotential of 0.25 V for Zn-MXene-Li anode was still maintained at a high current density of 16 mA cm^{-2} (Fig. 10d), which is lower than that of most reported Li-based composites. Moreover, the plating-stripping curves were still stable in the range of 5-40 mAh cm^{-2} at 1 mA cm^{-2} and lithium metal still tended to grow on the surface of Zn-MXene films (Fig. 10e). Besides, the surface integrity of the Zn-MXene film remained intact after repeated folding and twisting, indicating excellent flexibility. In parallel, Feng et al.[89] anchored ultra-fine and strong Au layers on MXene paper to design 3D flexible MXene@Au host by ion sputtering method. The flexible 3D MXene@Au@Li anode showed significantly enhanced performance with high-capacity retention of 98.47% even after 200 cycles and good rate capability, which could also be extended to other metal cell systems.

In addition to metal nanoseeds modifications, nonmetallic atoms-doped MXene materials as Li metal bodies have been widely reported and significant results have been achieved. In Xin's study[90], boron (B)-doped MXene@Li electrode demonstrated Li^+ plating/stripping efficiency, associated with larger electronegativity of B. As we all know, elements with a large electronegativity correspond to strong electron-attracting ability. Thus, the ability of negative charge (e.g., —F and —O) to adsorb Li near B was enhanced. So B ions could provide more active sites to induce uniform deposition of Li (Fig. 10f).

Finally, B-doped $Ti_3C_2T_x$@Li anode exhibited good cyclic stability with high CE in different test conditions. The full cells composed of B-doped MXene@Li as anode matching $LiFePO_4$ cathode emerged preferable cycling stability and rate performance (Fig. 10g). In view of this concept, Niu's group[91] doped BF_3 to single layer Ti_3C_2-MXene, which enhanced interfacial stability between MXene surface and electrolyte. Meanwhile, BF_3-MXene layer combining *in-situ*-formed lithium carboxylate organic layer supported rapid Li-ion diffusion, resulting in a long cycling capability of large-sized full-cell.

Red phosphorus is often used as modifier for alkali metal anodes due to its high theoretical specific capacity (2 600 mAh g^{-1}) and its role in promoting the migration of alkali metal ions. In addition, red P alloys Li metal to form Li_3P, which reduces the interfacial resistance, accelerating the reaction kinetics and homogenizing Li deposition. However, the low conductivity characteristic prevents P from contributing to the battery anodes. Huang et al.[92] designed iodine-doped red P to prepare MXene@iodine-doped red phosphorus paper (MXene@RP) based on the advantages of iodine alleviating low conductivity. The uniform distribution of iodine-doped red phosphorus particles between MXene layers provided more nucleation sites for regulating the nucleation and growth of lithium (Fig. 10h, j and k). And the formation of Ti-O-P bonds maintained the stability of the material to ensure long battery life (Fig. 10m). LFP|MXene@RP@Li full battery maintained a Coulombic efficiency of 98.6% and a capacity retention rate of 81.4% for 600 cycles at 4 C, which proposed a feasible scheme for the development of high energy and high cycle efficiency batteries.

4 Conclusion and outlook

This review provided an overview of the latest research progress on developing MXene-based lithium metal hosts. Various synthesis methods of MXenes, including hydrofluoric-based solution etching, hydrofluoric-free solution etching, molten salt etching, CVD method and so on, were systematically introduced. As hosts, pure 2D structured MXenes exhibited robust mechanical strength, high flexibility and could be easily transformed into different 3D frameworks, which enables multiple routes for Li^+ transmission. In general, MXenes materials hold promise as effective hosts for lithium metal, which contributes to the development of high-performance lithium-metal batteries. Meanwhile, the multifunctional functional groups on the surface of MXene provided more nucleation sites for Li deposition, pro-

moting dendrite-free lithium growth. In recent years, researchers devoted to doping various external reagents to functionalize MXene hosts, including graphenes, reduced graphene oxides, carbon nanotubes, carbon nanofibers, ordered mesoporous carbons, lithiophilic metal nanoseeds (Zn, Au etc.) and nonmetallic atoms (B, P, etc.). The modified MXenes are expected to be applied in high-energy-density lithium metal batteries.

Although great progress has been made in the research of MXenes materials, there is still a long way to go in the commercial applications of MXenes materials in practical battery systems:

(1) The surface terminations play crucial roles in the nucleation and deposition behaviors of Li. It is reported that —OH exhibits Li lithiophobicity, while —O and —F functional groups could act as lithiophilic sites for Li uniform nucleation and growth. The comprehensive effects of two or more surface functional groups still needs further understanding. In addition, more synthesis methods are expected to be designed to produce MXene with other terminations, enriching the MXene material family.

(2) The electrochemical stability of MXene/Li composite anode at high current density should be paid attention. Single strategy could not solve all the problems of lithium metal anodes. It is reasonable to combine multiple methods (artificial SEI layer, electrolyte additives, etc.) to design lithium metal batteries with higher energy density and longer cycle life.

(3) Combine theoretical calculations, machine simulations and advanced characterization technologies to reveal the evolution of lithium metal negative electrode during the process of charging and discharging, and establish more key parameters of lithium metal battery to provide research directions for the next generation rechargeable batteries.

Introducing MXene materials into LMA could not only effectively address the problems of dendrite and volume expansion, but also promote the development of green energy storage systems, providing feasible strategies for developing the LMBs with high-energy densities and high security.

Declaration of Competing Interest

The authors declare no competing financial interest.

Acknowledgments

The authors appreciate the support from National Natural Science Foundation of China (52072256), Key R & D program of Shanxi Province (202102030201006, 202202070301016), Central guide local science and technology development funding program (YDZJSX2021B005), Shanxi Province Science and Technology Program unveiled bidding program (20201101016), Science and technology innovation base construction project of Shanxi Province (YDZJSX2022B003), Fundamental Research Program of Shanxi Province (20210302124308). Shanxi Province Teaching Reform Project (2021YJJG046).

References

[1] Winter, M, Barnett, B, Xu, K. Before Li ion batteries[J]. Chemical Reviews, 2018, 118: 11433-11456.

[2] Wu F, Liu M Q, Li Y, et al. High-mass-loading electrodes for advanced secondary batteries and supercapacitors[J]. Electrochemical Energy Reviews, 2021, 4: 382-446.

[3] Zhao J, Lian J, Zhao Z, et al. A review of in-situ techniques for probing active sites and mechanisms of electrocatalytic oxygen reduction reactions[J]. Nano-Micro Letters, 2023, 15: 19.

[4] Cheng X Q, Li H J, Zhao Z X, et al. The use of in-situ Raman spectroscopy in investigating carbon materials as anodes of alkali metal-ion batteries[J]. New Carbon Materials, 2021, 36: 93-103.

[5] Cheng X, Bai Q, Li H, et al. Nanoconfined SnS_2 in robust SnO_2 nanocrystals building heterostructures for stable sodium ion storage[J]. Chemical Engineering Journal, 2022, 442: 136222.

[6] Li H, Wang X, Zhao Z, et al. Microstructure controlled synthesis of Ni, N-codoped CoP/carbon fiber hybrids with improving reaction kinetics for superior sodium storage[J]. Journal of Materials Science & Technology, 2022, 99: 184-192.

[7] Chu S, Cui Y, Liu N. The path towards sustainable energy[J]. Nature Materials, 2017, 16: 16-22.

[8] Trahey L, Brushett F R, Balsara N P, et al. Energy storage emerging: A perspective from the joint center for energy storage research[J]. Proceedings of the National Academy of Sciences, 2020, 117: 12550-12557.

[9] Qiao Y, Yang H J, Chang Z, et al. A high-energy-density and long-life initial-anode-free lithium battery enabled by a Li_2O sacrificial agent[J]. Nature Energy, 2021, 6: 653-662.

[10] Tang Y X, Zhang Y Y, Li W L, et al. Rational material design for

ultrafast rechargeable lithium-ion batteries[J]. Chemical Society Reviews, 2015, 44: 5926-5940.

[11] Ciez R E, Whitacre J F. The cost of lithium is unlikely to upend the price of Li-ion storage systems[J]. Journal of Power Sources, 2016, 320: 310-313.

[12] Huang B, Pan Z F, Su X Y, et al. Recycling of lithium-ion batteries: Recent advances and perspectives[J]. Journal of Power Sources, 2018, 399: 274-286.

[13] Placke T, Kloepsch R, Dühnen S, et al. Lithium ion, lithium metal, and alternative rechargeable battery technologies: The odyssey for high energy density[J]. Journal of Solid State Electrochemistry, 2017, 21: 1939-1964.

[14] Wang C Y, Liu T, Yang X G, et al. Fast charging of energy-dense lithium-ion batteries[J]. Nature, 2022, 611: 485-490.

[15] Wei C L, Tao Y, Fei H F, et al. Recent advances and perspectives in stable and dendrite-free potassium metal anodes[J]. Energy Storage Materials, 2020, 30: 206-227.

[16] Gao M, Li H, Xu L, et al. Lithium metal batteries for high energy density: Fundamental electrochemistry and challenges[J]. Journal of Energy Chemistry, 2021, 59: 666-687.

[17] Liu B, Zhang J G, Xu W. Advancing lithium metal batteries[J]. Joule, 2018, 2: 833-845.

[18] Zhang H G, Ning H, Busbee J, et al. Electroplating lithium transition metal oxides[J]. Science Advances, 2017, 3: e1602427.

[19] Meng Q, Deng B, Zhang H, et al. Heterogeneous nucleation and growth of electrodeposited lithium metal on the basal plane of single-layer graphene[J]. Energy Storage Materials, 2019, 16: 419-425.

[20] Yan X, Lin L, Chen Q, et al. Multifunctional roles of carbon-based hosts for Li-metal anodes: A review[J]. Carbon Energy, 2021, 3: 303-329.

[21] Li C, Zhang S, Miao X, et al. Designing lithium argyrodite solid-state electrolytes for high-performance all-solid-state lithium batteries[J]. Batteries & Supercaps, 2022, 5: e202100288.

[22] Yan C L. Realizing high performance of solid-state lithium metal batteries by flexible ceramic/polymer hybrid solid electrolyte[J]. Rare Metals, 2020, 39: 458-459.

[23] Alexander G V, Indu M S, Kamakshy S, et al. Development of stable and conductive interface between garnet structured solid electrolyte and lithium metal anode for high performance solid-state battery[J]. Electrochimica Acta, 2020, 332: 135511.

[24] Chen K H, Wood K N, Kazyak E, et al. Dead lithium: Mass transport effects on voltage, capacity, and failure of lithium metal anodes[J]. Journal of Materials Chemistry A, 2017, 5: 11671-11681.

[25] Phattharasupakun N, Wutthiprom J, Duangdangchote S, et al. A 3D free-standing lithiophilic silver nanowire aerogel for lithium metal batteries without lithium dendrites and volume expansion: In operando X-ray diffraction[J]. Chemical Communications, 2019, 55: 5689-5692.

[26] Cheng X B, Zhang R, Zhao C Z, et al. Toward safe lithium metal anode in rechargeable batteries: A review[J]. Chemical Reviews, 2017, 117: 10403-10473.

[27] Le T, Liang Q, Chen M, et al. A triple-gradient host for long cycling lithium metal anodes at ultrahigh current density[J]. Small, 2020, 16: 2001992.

[28] Zhang X L, Ruan Z Q, He Q T, et al. Three-dimensional (3D) nanostructured skeleton substrate composed of hollow carbon fiber/carbon nanosheet/ZnO for stable lithium anode[J]. ACS Applied Materials & Interfaces, 2021, 13: 3078-3088.

[29] Qiao L, Zhang R, Li Y, et al. Super-assembled hierarchical and stable N-doped carbon nanotube nanoarrays for dendrite-free lithium metal batteries[J]. ACS Applied Energy Materials, 2022, 5: 815-824.

[30] Dong P, Zhang X, Cha Y, et al. Corrigendum to “In situ surface protection of lithium metal anode in lithium-selenium disulfide batteries with ionic liquid-based electrolytes”[J]. Nano Energy, 2020, 72: 104722.

[31] Liu Y, Wu Y, Zheng J, et al. Silicious nanowires enabled dendrites suppression and flame retardancy for advanced lithium metal anodes[J]. Nano Energy, 2021, 82: 105723.

[32] Liu Y Y, Tzeng Y K, Lin D C, et al. An ultrastrong double-layer nanodiamond interface for stable lithium metal anodes[J]. Joule, 2018, 2: 1595-1609.

[33] Zheng G Y, Lee S W, Liang Z, et al. Interconnected hollow carbon nanospheres for stable lithium metal anodes[J]. Nature Nanotechnology, 2014, 9: 618-623.

[34] Ma Y, Gu Y, He Y, et al. Fast-charging and dendrite-free lithium metal anode enabled by partial lithiation of graphene aerogel[J]. Nano Research, 2022, 15: 9792-9799.

[35] Qin R, Shan G, Hu M, et al. Two-dimensional transition metal carbides and/or nitrides (MXenes) and their applications in sensors[J]. Materials Today Physics, 2021, 21: 100527.

[36] Zhou C, Zhao X, Xiong Y, et al. A review of etching methods of MXene and applications of MXene conductive hydrogels[J]. European Polymer Journal, 2022, 167: 111063.

[37] Iqbal N, Ghani U, Liao W, et al. Synergistically engineered 2D MXenes for metal-ion/Li-S batteries: Progress and outlook[J]. Materials Today Advances, 2022, 16: 100303.

[38] Choi E, Lee J, Kim Y J, et al. Enhanced stability of $Ti_3C_2T_x$ MXene enabled by continuous ZIF-8 coating[J]. Carbon, 2022, 191: 593-599.

[39] Yin X, Jin J, Chen X, et al. Ultra-wear-resistant MXene-based composite coating via in situ formed nanostructured tribofilm[J]. ACS Applied Materials & Interfaces, 2019, 11: 32569-32576.

[40] Ding J, Zhao H, Yu H. Structure and performance insights in carbon dots-functionalized MXene-epoxy ultrathin anticorrosion coatings[J]. Chemical Engineering Journal, 2022, 430: 132838.

[41] Li B, Zhang D, Liu Y, et al. Flexible Ti_3C_2 MXene-lithium film with lamellar structure for ultrastable metallic lithium anodes[J]. Nano Energy, 2017, 39: 654-661.

[42] Ding L, Wei Y, Wang Y, et al. A two-dimensional lamellar membrane: MXene nanosheet stacks[J]. Angewandte Chemie International Edition, 2017, 56: 1825-1829.

[43] Ghosh K, Pumera M. MXene and MoS_{3-x} coated 3D-printed hybrid electrode for solid-state asymmetric supercapacitor[J]. Small Methods, 2021, 24: 2100451.

[44] Aakyiir M, Tanner B, Yap P L, et al. 3D printing interface-modified

PDMS/MXene nanocomposites for stretchable conductors[J]. Journal of Materials Science & Technology, 2022, 117: 174-182.

[45] Zhao F, Zhai P, Wei Y, et al. Constructing artificial SEI layer on lithiophilic MXene surface for high-performance lithium metal anodes[J]. Advanced Science, 2022, 9: 2103930.

[46] Guo D, Ming F, Shinde D B, et al. Covalent assembly of two-dimensional COF-on-MXene heterostructures enables fast charging lithium hosts[J]. Advanced Functional Materials, 2021, 31: 2101194.

[47] Wei C L, Tao Y, An Y L, et al. Recent advances of emerging 2D MXene for stable and dendrite-free metal anodes[J]. Advanced Functional Materials, 2020, 30(45): 2004613.

[48] Zhan X X, Si C, Zhou J, et al. MXene and MXene-based composites: Synthesis, properties and environment-related applications[J]. Nanoscale Horizons, 2020, 5(2): 235-258.

[49] Ha S, Kim D, Lim H K, et al. Lithiophilic MXene-guided lithium metal nucleation and growth behavior[J]. Advanced Functional Materials, 2021, 31(32): 2101261.

[50] Zia A, Cai Z P, Naveed A B, et al. MXene, silicene and germanene: Preparation and energy storage applications[J]. Materials Today Energy, 2022, 30: 101144.

[51] Zhang S, Ying H, Huang P, et al. Hierarchical utilization of raw $Ti_3C_2T_x$ MXene for fast preparation of various $Ti_3C_2T_x$ MXene derivatives[J]. Nano Research, 2022, 15(3): 2746-2755.

[52] Lucero N, Vilcarino D, Datta D, et al. The roles of MXenes in developing advanced lithium metal anodes[J]. Journal of Energy Chemistry, 2022, 69: 132-149.

[53] Naguib M, Kurtoglu M, Presser V, et al. Two-dimensional nanocrystals produced by exfoliation of Ti_3AlC_2[J]. Advanced Materials, 2011, 23(37): 4248-4253.

[54] Wei Y, Zhang P, Soomro R A, et al. Advances in the synthesis of 2D mxenes[J]. Advanced Materials, 2021, 33(39): 2103148.

[55] Alwarappan S, Nesakumar N, Sun D, et al. 2D metal carbides and nitrides (MXenes) for sensors and biosensors[J]. Biosensors and Bioelectronics, 2022, 205(2022): 113943.

[56] Zhang Q K, Zhang Y C, Wei C L, et al. Highly reversible lithium metal-organic battery enabled by a freestanding MXene interlayer[J]. Journal of Power Sources, 2022, 521: 230963.

[57] Ghazaly A E, Ahmed H, Rezk A R, et al. Ultrafast, one-step, salt-solution-based acoustic synthesis of Ti_3C_2 MXene[J]. ACS Nano, 2021, 15: 4287-4293.

[58] Feng A, Yu Y, Wang Y, et al. Two-dimensional MXene Ti_3C_2 produced by exfoliation of Ti_3AlC_2[J]. Materials & Design, 2017, 114: 161-166.

[59] Halim J, Lukatskaya M R, Cook K M, et al. Transparent conductive two-dimensional titanium carbide epitaxial thin films[J]. Chemistry of Materials, 2014, 26: 2374-2381.

[60] Liu F F, Zhou A G, Chen J F, et al. Preparation of Ti_3C_2 and Ti_2C MXenes by fluoride salts etching and methane adsorptive properties[J]. Applied Surface Science, 2017, 416: 781-789.

[61] Alhabeb M, Maleski K, Anasori B, et al. Guidelines for synthesis and processing of two-dimensional titanium carbide ($Ti_3C_2T_x$ MXene)[J]. Chemistry of Materials, 2017, 29: 7633-7644.

[62] Alhabeb M, Maleski K, Mathis T S, et al. Selective etching of silicon from Ti_3SiC_2 (MAX) to obtain 2D titanium carbide (MXene)[J]. Angewandte Chemie-International Edition, 2018, 57: 5444-5448.

[63] Zhou J, Zha X H, Chen F Y, et al. A two-dimensional zirconium carbide by selective etching of Al_3C_3 from nanolaminated $Zr_3Al_3C_5$[J]. Angewandte Chemie-International Edition, 2016, 55: 5008-5013.

[64] Mashtalir O, Naguib M, Mochalin V N, et al. Intercalation and delamination of layered carbides and carbonitrides[J]. Nature Communications, 2013, 4: 1716.

[65] Yang S, Zhang P P, Wang F X, et al. Fluoride-free synthesis of two-dimensional titanium carbide (MXene) using a binary aqueous system[J]. Angewandte Chemie-International Edition, 2018, 57: 15491-15495.

[66] Li T F, Yao L L, Liu Q L, et al. Fluorine-free synthesis of high-purity $Ti_3C_2T_x$ (T=OH, O) via alkali treatment[J]. Angewandte Chemie-International Edition, 2018, 57: 6115-6119.

[67] Li M, Lu J, Luo K, et al. Element replacement approach by reaction with lewis acidic molten salts to synthesize nanolaminated MAX phases and MXenes[J]. Journal of the American Chemical Society, 2019, 141: 4730-4737.

[68] Li Y, Shao H, Lin Z, et al. A general Lewis acidic etching route for preparing MXenes with enhanced electrochemical performance in non-aqueous electrolyte[J]. Nature Materials, 2020, 19: 894-899.

[69] Urbankowski P, Anasori B, Makaryan T, et al. Synthesis of two-dimensional titanium nitride Ti_4N_3 (MXene)[J]. Nanoscale, 2016, 8: 11385-11391.

[70] Kamysbayev V, Filatov A S, Hu H C, et al. Covalent surface modifications and superconductivity of two-dimensional metal carbide MXenes[J]. Science, 2020, 369: 979-983.

[71] Xu C, Wang L, Liu Z, et al. Large-area high-quality 2D ultrathin Mo_2C superconducting crystals[J]. Nature Materials, 2015, 14: 1135-1141.

[72] Wang Z, Kochat V, Pandey P, et al. Metal immiscibility route to synthesis of ultrathin carbides, borides and nitrides[J]. Advanced Materials, 2017, 29: 1700364.

[73] Wang L, Xu C, Liu Z, et al. Magnetotransport properties in high-quality ultrathin two-dimensional superconducting Mo_2C crystals[J]. ACS Nano, 2016, 10: 4504-4510.

[74] Hong Y L, Liu Z B, Wang L, et al. Chemical vapor deposition of layered two-dimensional $MoSi_2N_4$ materials[J]. Science, 2020, 369: 670-674.

[75] Mei J, Ayoko G A, Hu C, et al. Two-dimensional fluorine-free mesoporous Mo_2C MXene via UV-induced selective etching of Mo_2Ga_2C for energy storage[J]. Sustainable Materials and Technologies, 2020, 25: e00156.

[76] Ljubek G, Kralj M, Kraljić Roković M. Fluorine-free mechanochemical synthesis of MXene[J]. Materials Science and Technology, 2023: 1-5.

[77] L. Liu, H. Zschiesche, M. Antonietti, et al. In situ synthesis of MXene with tunable morphology by electrochemical etching of MAX phase prepared in molten salt[J]. Advanced Energy Materials, 2023, 13: 2203805.

[78] Chen Q, Wei Y, Zhang X, et al. Vertically aligned MXene

nanosheet arrays for high-rate lithium metal anodes[J]. Advanced Energy Materials, 2022, 12: 2200072.

[79] Cao Z J, Zhu Q, Wang S, et al. Perpendicular MXene arrays with periodic interspaces toward dendrite-free lithium metal anodes with high-rate capabilities[J]. Advanced Functional Materials, 2020, 30: 1908075.

[80] Shen K, Li B, Yang S. 3D printing dendrite-free lithium anodes based on the nucleated MXene arrays[J]. Energy Storage Materials, 2020, 24: 670-675.

[81] Shi H, Zhang C J, Lu P, et al. Conducting and lithiophilic MXene/graphene framework for high-capacity, dendrite-free lithium-metal anodes[J]. ACS Nano, 2019, 13: 14308-14318.

[82] Fang Y, Zhang Y, Zhu K, et al. Lithiophilic three-dimensional porous $Ti_3C_2T_x$-rGO membrane as a stable scaffold for safe alkali metal (Li or Na) anodes[J]. ACS Nano, 2019, 13: 14319-14328.

[83] Zheng W, Zhang P, Chen J, et al. In situ synthesis of CNTs@Ti_3C_2 hybrid structures by microwave irradiation for high-performance anodes in lithium ion batteries[J]. Journal of Materials Chemistry A, 2018, 6: 3543-3551.

[84] Zhang S, Liu H, Cao B, et al. An MXene/CNTs@P nanohybrid with stable Ti-O-P bonds for enhanced lithium ion storage[J]. Journal of Materials Chemistry A, 2019, 7: 21766-21773.

[85] Liu Y, Sun C, Lu Y, et al. Lamellar-structured anodes based on lithiophilic gradient enable dendrite-free lithium metal batteries with high capacity loading and fast-charging capability[J]. Chemical Engineering Journal, 2023, 451: 138570.

[86] Tao M, Li W, Luo P, et al. High utilization lithium metal anode constructed by allocatable MXene foam container[J]. Journal of Power Sources, 2022, 551: 232089.

[87] Pourali Z, Sovizi M R, Yaftian M R. Two-dimensional $Ti_3C_2T_x$/CMK-5 nanocomposite as high performance anodes for lithium batteries[J]. Journal of Alloys and Compounds, 2018, 738: 130-137.

[88] Gu J, Zhu Q, Shi Y, et al. Single zinc atoms immobilized on MXene ($Ti_3C_2Cl_x$) layers toward dendrite-free lithium metal anodes[J]. ACS Nano, 2020, 14: 891-898.

[89] Qian Y, Wei C, Tian Y, et al. Constructing ultrafine lithiophilic layer on MXene paper by sputtering for stable and flexible 3D lithium metal anode[J]. Chemical Engineering Journal, 2021, 421: 129685.

[90] Wu N, Zhang Q Y, Guo Y J, et al. Boron-doped three-dimensional MXene host for durable lithium-metal anode[J]. Rare Metals, 2022, 41: 2217-2222.

[91] Shang M, Shovon O G, Wong F E Y, et al. A BF_3-doped MXene dual-layer interphase for a reliable lithium-metal anode[J]. Advanced Materials, 2023, 35: 2210111.

[92] Na Z, Li W, Li L, et al. Conductive iodine-doped red phosphorus enabled dendrite-free lithium deposition on MXene matrix[J]. Small, 2022, 18: 2204341.